


Cite this: *RSC Adv.*, 2025, 15, 40968

# Reverse micelle-mediated synthesis of precision-controlled FeS nanospheres and their role in tailored FeS@PANI nanocomposites

Nargis Khatun,<sup>a</sup> Sk Meheubub Rahaman,<sup>\*a</sup> Bipasha Saha,<sup>b</sup> Trishna Mandal,<sup>a</sup> Arnab Patra,<sup>a</sup> Mahasweta Nandi,<sup>id b</sup> Dileep Kumar,<sup>id cd</sup> Abhik Chatterjee<sup>e</sup> and Bidyut Saha<sup>id \*a</sup>

In this study, we introduce a novel approach that combines reverse micelle-mediated synthesis of FeS nanospheres with Pickering emulsion-templated polymerization, offering the unveiling of an unexplored strategy for precise control over the size and morphology of FeS@PANI nanocomposites. Unlike prior studies, which did not focus the role of Pickering emulsions in directing polymer growth, this present approach leverages emulsion interface stabilization and micellar confinement to regulate polymerization dynamics and composite architecture. Using reverse micelles composed of SPAN 80, 1-butanol, toluene, and FeS, five distinct water-to-surfactant ( $W_0$ ) mole ratios (5, 10, 15, 20, and 30) were explored to precisely control the size and morphology of FeS nanospheres. TEM and FESEM analyses, along with PDI evaluations, demonstrate that increasing the water content ( $W_0 = 5$  to 30) leads to a progressive increase in nanosphere size. At lower  $W_0$  values, strong interactions between surfactants and water molecules slow down intermicellar exchange, resulting in the formation of small, monodisperse nanospheres with enhanced stability. These nanospheres readily accumulate at the toluene–water interface, effectively encapsulating the non-aqueous phase. Nanospheres synthesized at  $W_0 = 5$  were then employed in Pickering emulsion formation, achieving maximum stability at 0.075 wt% FeS. In an exciting breakthrough, these stable Pickering emulsions facilitated the polymerization of aniline, leading to the successful formation of FeS@PANI nanocomposites, as confirmed by PXRD, UV, IR, and  $^1\text{H}$ -NMR analyses. TEM and FESEM images reveal that FeS-stabilized emulsions control the size and morphology of polyaniline with precision. At 0.075 wt% FeS, spherical FeS@PANI nanocomposites of 40 nm were achieved, while the absence of FeS led to aggregated, distorted structures. This work highlights the transformative potential of FeS nanospheres, not only as emulsion stabilizers but also as key regulators of polymeric nanocomposite morphology, paving the way for advanced materials in diverse applications.

Received 29th May 2025  
Accepted 21st October 2025

DOI: 10.1039/d5ra03785a

rsc.li/rsc-advances

## 1. Introduction

In recent years, nanomaterials research has seen remarkable growth driven by the demand for precisely engineered structures with unique properties tailored for diverse applications

such as energy storage, catalysis, drug delivery, and electronics.<sup>1,2</sup> Hybrid nanocomposites, notable for their multi-functional properties, have emerged as integral components in these fields.<sup>1,2</sup> Controlling the size, shape, and composition of nanoparticles is key to developing high-performance materials.<sup>3</sup> Reverse micellar systems have become a versatile platform for such controlled synthesis, utilizing nanoscale confinement and templating effects inherent to these assemblies.<sup>4,5</sup>

Reverse micelles are water-in-oil (W/O) microemulsions where nanoscopic aqueous domains are stabilized by surfactants (and sometimes additional stabilizers cosurfactants is required) within a continuous organic phase.<sup>5–7</sup> A critical parameter in these systems is the water-to-surfactant molar ratio ( $W_0$ ), which dictates the size and dynamics of the aqueous core.<sup>6</sup> This confined nanoreactor environment promotes the formation of monodisperse nanoparticles with controllable size and shape.<sup>7–10</sup> Therefore, a central aim is to investigate the influence of the  $W_0$  on FeS nanosphere characteristics,

<sup>a</sup>Materials Chemistry Laboratory, Department of Chemistry, The University of Burdwan, Golapbag, Burdwan-713104, West Bengal, India. E-mail: bsaha@chem.buruniv.ac.in; smrahaman@scholar.buruniv.ac.in; meheububchemistry@gmail.com; Tel: +91 9476341691; +91 8016288873

<sup>b</sup>Integrated Science Education and Research Centre, Siksha Bhavana, Visva-Bharati University, Santiniketan-731235, India

<sup>c</sup>Laboratory for Chemical Computation and Modeling, Institute for Computational Science and Artificial Intelligence, Van Lang University, Ho Chi Minh City 70000, Vietnam. E-mail: kumar.dileep@vlu.edu.vn

<sup>d</sup>Faculty of Applied Technology, School of Technology, Van Lang University, Ho Chi Minh City 70000, Vietnam

<sup>e</sup>Department of Chemistry, Raiganj University, Uttar Dinajpur, Raiganj, 733134, West Bengal, India



including size, morphology, and emulsion stabilization ability.<sup>10</sup> Transmission electron microscopy (TEM) provided insights into the size and morphology of the nanoparticles.<sup>8</sup> Field emission scanning electron microscopy (FESEM) was employed to examine surface morphology and overall particle architecture.<sup>8,11</sup> Additionally, polydispersity index (PDI) analysis was used to assess the size distribution and uniformity of the nanoparticles across different  $W_0$  conditions.<sup>8–13</sup> Several earlier discussions suggested that lower  $W_0$  values restrict intermicellar exchange due to stronger surfactant–water interactions, yielding stable, monodisperse nanoparticles. In contrast, higher  $W_0$  values promote more intermicellar exchange, resulting in larger, polydisperse nanoparticles. These insights are vital for designing reverse micellar systems tailored for specific nanoparticle properties. Now, the controlled metal sulfide nanoparticles, synthesized *via* this reverse micellar approach exhibit excellent electrical, optical, and catalytic behaviours.<sup>8–13</sup> Among these, iron sulfide (FeS) nanoparticles have attracted considerable interest due to their potential in energy conversion, environmental remediation, and catalysis.<sup>9,14</sup> Interestingly, in recent times such reverse micellar synthesised nanoparticles are utilised in Pickering emulsion formulations after suitable modifications. Rahaman *et al.* demonstrated the use of reverse micelle-mediated Co(OH)<sub>2</sub> nanoparticles for stabilizing toluene–water Pickering emulsions.<sup>15</sup> Similarly, Mandal *et al.* employed lanthanum phosphate nanoparticles as effective solid stabilizers in such emulsions.<sup>16</sup> Building on these approaches, the present study utilizes reverse micelle-templated FeS nanoparticles for the stabilization of toluene–water Pickering emulsions, introducing a new class of inorganic nanostructures for emulsion interface engineering.

Pickering emulsions, stabilized by solid particles, offer enhanced stability over surfactant-based systems.<sup>10,12</sup> Their performance depends on particle size, shape, and wettability, tunable *via* reverse micelle synthesis.<sup>12</sup> Inorganic particles like SiO<sub>2</sub>, Al<sub>2</sub>O<sub>3</sub>, and TiO<sub>2</sub> enable control over emulsion stability.<sup>13,14,17–20</sup> However, there is a gap in the literature and lack of extensive investigations regarding the use of W/O microemulsions mediated non-traditional nanoparticles in Pickering emulsion stabilization. Ultimately, this study adds significant value to the exploration of this previously unexplored area of colloidal science and builds an effective bridge between microemulsions and Pickering emulsions, two integral types of emulsions. Therefore, through addressing this research gap, the present study explores the application of FeS nanoparticles, synthesized *via* reverse micellar techniques, as stabilizers in Pickering emulsions. These FeS nanospheres offer a promising link between controlled nanoparticle synthesis and functional emulsion stabilization.

Pickering emulsion polymerization of aniline remains relatively unexplored. Recent advances include composites like polyaniline/zinc-ferrite and polyaniline/MnO<sub>2</sub>/graphene synthesized *via* this method.<sup>21–24</sup> Here, in this study, a surfactant-free oil-in-water Pickering emulsion stabilized solely by FeS nanospheres is utilized to produce FeS@PANI polymeric nanocomposites through Pickering emulsion polymerization.

Spectroscopic analyses, including PXRD, UV-vis, FTIR, and <sup>1</sup>H-NMR, confirmed successful incorporation of FeS within the PANI matrix. FESEM and TEM studies highlighted that FeS nanospheres influence the composite morphology, yielding smaller and well-defined spherical particles compared to the aggregated and irregular structures formed without FeS. This morphological control translates into enhanced structural integrity and functional performance.<sup>25–27</sup>

Polyaniline (PANI), a well-established conducting polymer with tunable conductivity and environmental stability, forms a uniform, conductive matrix in FeS@PANI nanocomposites. Incorporation of FeS nanospheres improves both morphology and functional performance, with Pickering emulsion polymerization enabling controlled synthesis. FeS@PANI nanocomposites, have demonstrated potential in specific applications where surface activity and redox processes are critical. Due to the very low FeS loading (typically less than 1%), the composite's behaviour is largely dictated by PANI, with FeS offering limited but useful contributions, such as enhancing surface interactions or modifying electron transport characteristics. One practical use is in wastewater treatment, especially for removing toxic metal ions like Cr(VI) or Pb(II). In such cases, PANI provides active redox sites for capturing and transforming contaminants, while FeS can assist in improving removal efficiency through supplementary binding or redox interactions.<sup>28</sup> These composites have also been explored in chemical sensing, where PANI's electrical conductivity changes in response to analytes like hydrogen sulfide or ammonia, and FeS can fine-tune sensitivity and selectivity.<sup>29</sup> Additionally, they show promise in electromagnetic interference (EMI) shielding applications, where the electrical conductivity of PANI, combined with the dielectric or magnetic features of FeS, contributes to effective attenuation of EM radiation.<sup>30</sup> These use cases align well with the material's actual composition and functional limitations. Moreover, the emulsion-based, surfactant-free synthesis offers a clean, scalable route to multifunctional nanomaterials with tailored performance. However, it is to be highlighted that, enhancing PANI's structural and functional properties *via* nanoscale integration still remains challenging a challenging task. However, leveraging the interfacial stability and activity of FeS nanospheres, we successfully synthesized FeS@PANI composites with controlled morphology and improved functional attributes.<sup>31</sup> Consequently, the implications of this study extend beyond FeS@PANI synthesis, offering a framework for designing hybrid nanostructures using reverse micellar systems coupled with Pickering emulsions. The ability to finely tune nanoparticle size and interfacial properties *via* simple adjustments in  $W_0$  marks a significant advance in nanomaterials synthesis.<sup>32–34</sup> Furthermore, integrating FeS nanospheres with conducting polymers like PANI opens pathways for new functional materials applicable in energy storage, sensing, and environmental remediation.<sup>35–38</sup>

In summary, this work demonstrates the efficacy of microemulsions, particularly the role of the water-to-surfactant molar ratio in the controlled synthesis of nanoparticles. These nanoparticles are subsequently employed as solid stabilizers in Pickering emulsion formulations, which are then used in



a Pickering emulsion-based polymerization process to synthesize FeS@PANI, a highly conductive polymer. This study effectively bridges two promising branches of emulsion science, microemulsions and Pickering emulsions and opens a new direction in colloidal chemistry.

## 2. Experimental section

### 2.1 Materials

SPAN 80 (99%, AR, SRL-India), 1-butanol (99%, AR, SRL-India), toluene (99%, MERCK-India), ammonium ferrous sulphate (99%, AR, SRL-India), sodium sulfide (99%, AR, SRL-India), aniline (99%, AR, SRL-INDIA), potassium persulfate (99%, AR, Merck-India), HCl (Fisher Scientific). In order to produce all of the aqueous solutions used in the investigations, distilled water (Millipore, India) was used. A detailed information on used chemicals is given in Table 1.

### 2.2 Preparatory method of FeS nanoparticles at different $W_0$

Applying the reverse micellar method, FeS nanoparticle was synthesised. The procedure of preparation for W/O microemulsion is as follows:

Toluene was poured in a dry beaker having water and SPAN 80 in a pre-determined [water]/[surfactant] ( $W_0$ ) mole ratios (5, 10, 15, 20 and 30). The solution was thereafter placed in a digitally controlled ultrasonic bath (MC-109 SPL) and sonicated for 30 s. To achieve an optimum transparency, 1-butanol was slowly introduced to the turbid and viscous solution with continuous stirring. The system was given adequate time to reach

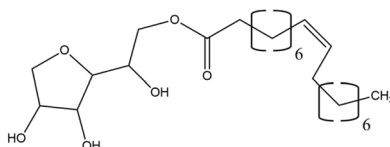
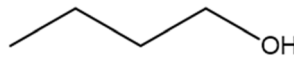
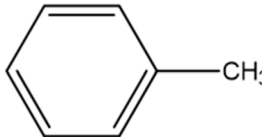
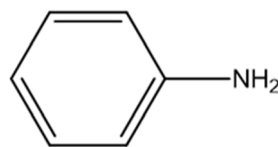
**Table 2** Volume percentages of each of the components of W/O microemulsion scaffolds at various  $W_0$  values

$W_0$	Volume percentages			
	Toluene	Water	SPAN 80	1-Butanol
5	65.96	1.32	6.33	26.39
10	63.78	1.28	3.05	31.89
15	63.61	1.27	2.04	33.08
20	62.34	1.25	1.50	34.91
30	56.94	1.13	0.91	41.02

equilibrium and once turbidity had vanished, it was not appeared again. Therefore, stable microemulsions were produced by using different amounts of 1-butanol for various  $W_0$ . The complete procedure was performed at a constant temperature of 303 K. The respective volume percentages of toluene, water, SPAN 80 and 1-butanol at various  $W_0$  values are represented in Table 2.

Now, in order to produce FeS nanoparticles a 1 M aqueous solution of  $\text{Fe}^{2+}$  and  $\text{S}^{2-}$  were separately added to the so-prepared W/O microemulsions scaffolds (having different  $W_0$ ), which also contained toluene as the non-polar phase, SPAN 80 as the surfactant, and 1-butanol as the cosurfactant. In other way, microemulsion I usually consisted of a 1 M solution of molar salt, while microemulsions II typically contained a 1 M solution of sodium sulfide. The two microemulsion systems were carefully combined and stirred on a magnetic stirrer (using a magnetic stirrer of model REMI) for 1 h at room temperature. The targeted product was separated using centrifugation

**Table 1** Detailed information on used chemicals

Chemicals	CAS No.	Source	Molar mass ( $\text{g mol}^{-1}$ )	Purity percentage	Structure
SPAN 80	1338-43-8	SRL-India	428.60	99%	
1-Butanol	71-36-3	SRL-India	74.12	99%	
Toluene	108-88-3	Merck-India	92.14	99%	
Ammonium ferrous sulphate	7783-85-9	SRL-India	392.14	99%	$(\text{NH}_4)_2\text{SO}_4 \cdot \text{FeSO}_4 \cdot 6\text{H}_2\text{O}$
Sodium sulfide	1313-82-2	SRL-India	78.0452	99%	$\text{Na}_2\text{S} \cdot 9\text{H}_2\text{O}$
Aniline	62-53-3	SRL-India	93.13	99%	
Potassium persulfate	7727-21-1	Merck-India	270.322	99%	$\text{K}_2\text{S}_2\text{O}_8$



(HERMLE Labortechnik GmbH) from the non-polar phase, surfactant, and cosurfactant. The process of centrifugation was performed at a speed of 4000 rpm for 15 min. The synthesized nanoparticles were allowed to dry in the open air, after cleaning with acetone. In this study, the nanoparticles were produced using five different types of microemulsions with  $W_0$  of 5, 10, 15, 20 and 30. The size of polar inner core of W/O microemulsions are altered with the variation in  $W_0$  values. Thereafter, it has a tremendous impact on the size of the targeted nanostructures.

### 2.3 Characterization of FeS nanoparticles

The crystallographic information of synthesised FeS nanoparticle was evaluated by using Powder X-ray diffraction (PXRD) on a Bruker D8 Advance diffractometer with Ni-filtered Cu K $\alpha$  radiation. FTIR spectrum data was acquired between 400 and 4000  $\text{cm}^{-1}$  using a KBr pellet method on a Shimadzu IRAffinity-1S FT-IR spectrophotometer. In a  $\text{N}_2$  environment, a TA SDT650 apparatus was used for a thermogravimetric analysis (TGA) with a temperature rise rate of 10  $^\circ\text{C min}^{-1}$ . Dynamic light scattering (DLS) (Malvern Zetasizer Nano ZS) was used to measure the polydispersity index (PDI) of FeS nanoparticles, formed from the reverse micellar core of different  $W_0$  values. The desired amount of aqueous colloidal dispersion of the so-synthesised FeS nanoparticle was placed in the quartz cell and the experiment was performed. A 30  $^\circ\text{C}$  test temperature was maintained in all sets of studies. Three separate measurements of PDI values were taken for each  $W_0$  value. Zeiss EM 912 U equipment with a 120 kV acceleration voltage was employed for the transmission electron microscope (TEM) study. Prior to place on the copper grids, the solid FeS nanostructures were initially dispersed in ethanol to produce a colloidal dispersion. In the bottom of the Petri dish, the copper grid was placed onto a piece of filter paper, just to prevent the agglomeration of nanoparticles. Field emission scanning electron microscope (FESEM) (Zeiss Gemini SEM 450) microstructures were analysed to assess the dimensions and morphology of the nanoparticles that were synthesized from different microemulsions medium. EDAX Ametek (Model: Element) was used to assess Energy dispersive X-ray (EDX).

### 2.4 Preparation and characterization of FeS stabilised Pickering emulsion

After adding a specific volume of pure water to a 5 mL glass vial (1 dram homoeopathy glass vial), a specific weight percentage (wt%) (0.0125, 0.025, 0.05, and 0.075) of FeS nanoparticles was added into it. Thereafter it was uniformly distributed *via* high ultrasonication (MC-109 SPL) for 5 min. 2 mL of toluene (acting as the non-polar phase) was then incorporated into the distribution and again sonicated for 5 min. Thereafter it was subjected to hand shaking for efficient emulsification. Nature of the emulsion (O/W or W/O type) was identified by using the drop test procedure, which involved submerging an emulsion drop in a large excess of aqueous phase or organic phase. Digital photographs of the produced emulsion were taken using a digital camera. Weswox-FM2000 optical microscopy was used to determine the micromorphology of the emulsion droplets.

The determination of the O/W type Pickering emulsion were identified through contact angle measurements, which provide insights into the wettability of the surface and the interfacial interactions between the oil, water, and substrate. The FeS powder samples were placed on a slide and flattened to create a uniform plane. The contact angle ( $\theta$ ) of a 5  $\mu\text{L}$  drop of pure water on the air-exposed substrate was determined by the sessile drop method (in a Kruss DSA25 drop shape analyzer). The slide was cleaned and polished after each measurement to prepare a new surface for the next concentration. The apparent viscosity of the Pickering emulsion (with wt% of 0.075, 0.05, 0.025, and 0.0125) was measured using an MCR 302 rheometer (Anton Paar), equipped with a temperature-controlled Peltier system and circulation pump. The viscosity was measured using a parallel plate setup with a 40 mm diameter, with shear rates varying between 1 and 500  $\text{s}^{-1}$ .

### 2.5 Synthesis of FeS@PANI composites in Pickering emulsion

A variable wt% (0.025 and 0.075) of FeS was taken in the water phase (2 mL), whereas the aniline-containing toluene made up the oil phase (2 mL). The two immiscible liquid pair were mixed and homogenised in a homogenizer for 2 min at 500 rpm to prepare the Pickering emulsion. The prepared emulsion was immersed in freezing water for about 30 min. Likewise, in a different system, a requisite amount of  $\text{K}_2\text{S}_2\text{O}_8$  ( $\text{K}_2\text{S}_2\text{O}_8/\text{aniline} = 1:1$ ) was added to a 1  $\text{mol L}^{-1}$  HCl solution and allowed to stand in an ice bath for 30 min. Potassium persulfate solution was then gently poured into the emulsion. The mixture was thereafter stirred in an ice water bath for 6 h to confirm the complete polymerization of aniline. The required product was isolated through centrifugation (centrifugation was continued for 15 min at a speed of 4000 rpm). To make a comparison, an additional set of polymerizations was performed by direct addition of acidic  $\text{K}_2\text{S}_2\text{O}_8$  to the aniline rather than using a Pickering emulsifier, FeS.

### 2.6 Characterization of FeS@PANI composites

The crystallographic characteristics of the synthesized FeS@PANI nanocomposite were meticulously examined using Powder X-ray Diffraction (PXRD), performed on a Bruker D8 Advance diffractometer equipped with Ni-filtered Cu K $\alpha$  radiation ( $\lambda = 1.5406 \text{ \AA}$ ), ensuring high-resolution phase identification and structural analysis. Using a Shimadzu 1800 UV-vis spectrophotometer, UV-Vis spectra of the FeS@PANI composites were taken between 200 and 800 nm. A Shimadzu FTIR-8400S spectrophotometer was employed to obtain the FTIR spectrum data of FeS@PANI nanocomposites within the range of 400 and 4000  $\text{cm}^{-1}$ . The samples were pelletized with spectroscopic grade KBr. By using a Bruker ASCEND-400 MHz spectrophotometer,  $^1\text{H}$  NMR measurements were carried out to determine the evaluations of FeS@PANI nanocomposites. Transmission electron microscopy (TEM) analysis was conducted using a Zeiss EM 912 U instrument operated at an accelerating voltage of 120 kV. To prepare the samples, the as-synthesized FeS@PANI nanocomposites were initially





ultrasonically dispersed in ethanol to form a stable colloidal suspension. A copper grid was carefully placed on a piece of filter paper at the bottom of a Petri dish to mitigate nanoparticle agglomeration during drying. Subsequently, a few drops of the dispersion were deposited onto the grid and allowed to dry under ambient conditions prior to imaging. The morphology of FeS@PANI was determined by field emission scanning electron microscopy (Zeiss Gemini SEM 450). Elemental composition analysis was carried out using Energy Dispersive X-ray Spectroscopy (EDX) integrated with an EDAX Ametek system (Model: Element), enabling precise identification of constituent elements within the nanocomposites.

### 3. Results and discussion

#### 3.1 Characterization of FeS nanoparticles

The structural characteristics of FeS nanoparticles were analyzed using powder X-ray diffraction (PXRD). The analysis was performed on a sample synthesized in a reverse micellar medium with  $W_0 = 5$ . The PXRD pattern, presented in Fig. 1a, exhibits primary diffraction peaks at  $2\theta = 15.73^\circ$  and  $32.02^\circ$ , corresponding to the (111) and (102) planes, respectively, as indexed by JCPDS File No. 76-0964.<sup>39</sup> The observed peaks are in

good agreement with the standard reference values, confirming the successful synthesis of FeS nanoparticles within the polar core of W/O microemulsion. Moreover, this PXRD result is consistent with previous findings reported by Asoufi *et al.* and supports the formation of FeS within the reverse micellar core.<sup>39</sup>

FTIR analysis has been used to characterize the functional groups of freshly prepared/synthesized FeS nanoparticles, obtained in the SPAN 80-based W/O microemulsion medium with  $W_0 = 5$ . Fig. 1b showed that, the vibrations of elongation and deformation of vibratory FeS nanoparticles are responsible for the strong bands appearing at  $684\text{--}414\text{ cm}^{-1}$ .<sup>40</sup> The O–H stretching mode arising from water absorption on the surface of FeS nanoparticles is correlated with the broad absorption peak at  $3202\text{--}3056\text{ cm}^{-1}$ .

Most of the thermal analyses involved noting changes in physical variables against the temperature. Thermal patterns can be used to assess the constituents, properties, and potential application of a material. Thermogravimetric analysis (TGA), a type of thermo-analytical test, is employed to analyze how temperature variations affect weight variations. A curve of TGA material's is a result of a specific combination of physio-chemical processes pertaining to chemical compositions and molecular structure.<sup>41</sup> TGA is frequently used to assess chemical

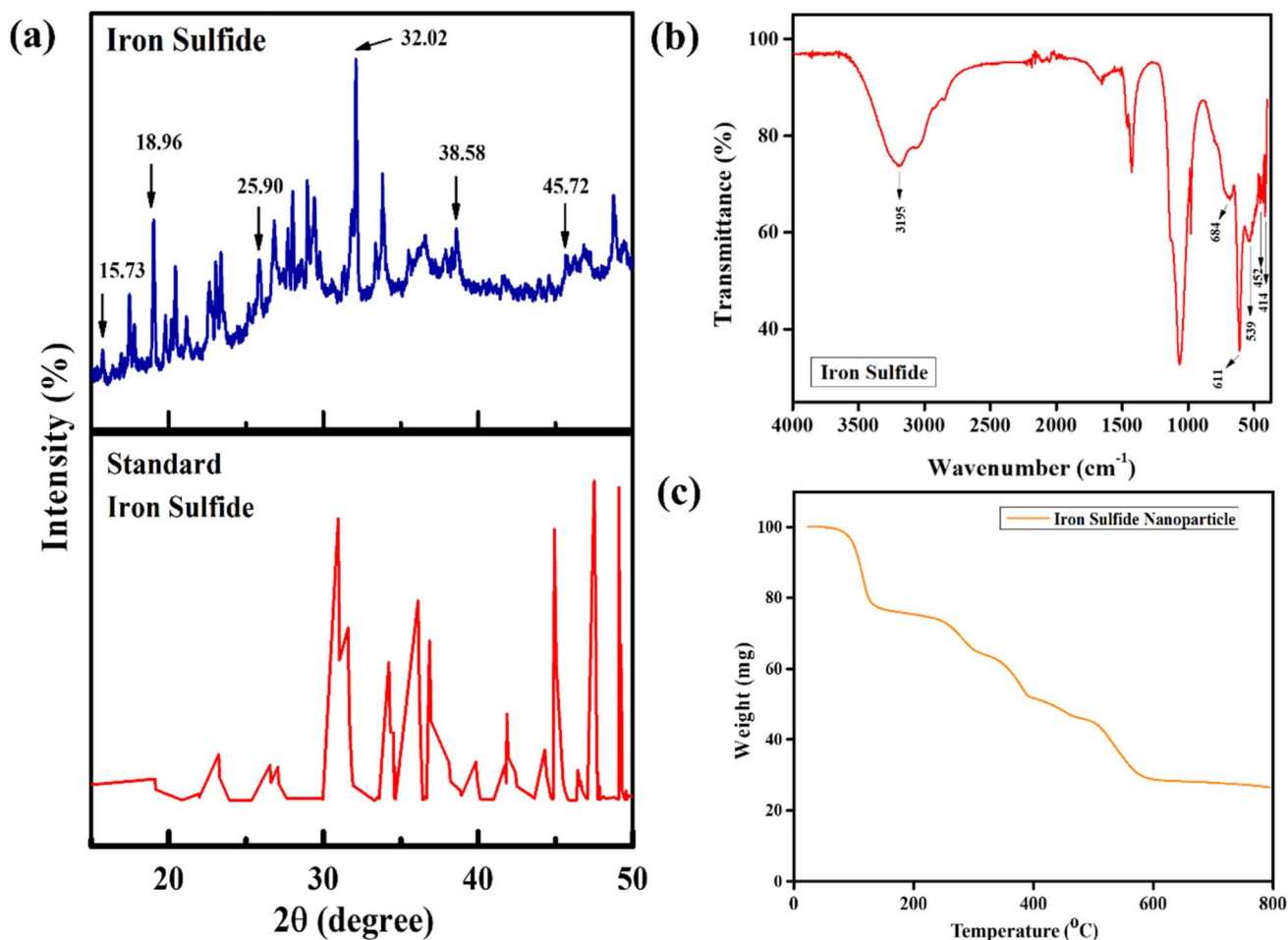


Fig. 1 (a) PXRD spectral analysis, (b) FTIR spectrum, (c) TGA curve of FeS nanospheres, synthesized from the polar core of W/O microemulsion medium of SPAN 80/toluene/1-butanol/FeS, having  $W_0 = 5$ .



alterations, including the amount of moisture, as well as degradation and disintegration processes.<sup>42</sup> Weight fluctuations arise from establishing or dissolving chemical and physical linkages, producing a more volatile or heavier material. The final TGA curve, with a temperature interval of 30–800 °C (shown in Fig. 1c), reveals the decreased quantity of FeS nanoparticles synthesized in toluene and 1-butanol-based microemulsion media.<sup>40</sup> TGA spectrum confirmed that water molecules adsorbed on the surface of the particles, vaporizes between 87 and 133 °C, resulting in a significant loss of weight. FTIR analysis has previously been used to identify the water molecules bounded to the surface of the FeS particles.<sup>40</sup> Subsequent to the initial rapid weight reduction regimen, a gradual weight loss is seen, with temperatures dropping from 240 °C to roughly 800 °C. It is assumed that the breakdown or deterioration of the nanostructures is the reason for this decreased rate of weight reduction.

Elemental mapping is employed to analyse the chemical constituents and assist in the sample purification of FeS

nanospheres. Fig. S1 illustrates the exclusive existence of Fe and S components in the synthesised nanoparticles after the reaction was completed at two distinct  $W_0$  ( $W_0 = 5$  and 30). Elemental mapping shows no trace of C, N, or O, confirming that the synthesized nanoparticles have been completely isolated from the microemulsion media and are free from impurities. Moreover, the EDX spectrum of FeS nanoparticles for every set of  $W_0$  is shown in Fig. S2 and it confirmed the presence of peaks related to Fe and S only. No other impurity related peaks (appeared due to the employed surfactants and cosurfactants) are found. It's therefore suggested that the complete separation of targeted particles from every set of reverse micellar scaffolds.

### 3.2 Examining the impact of water-to-surfactant mole ratio ( $W_0$ ) on the evaluated FeS nanospheres

The present study thoroughly examines the impact of  $W_0$  on the synthesis of FeS nanoparticles. Primarily three different technologies, TEM, FESEM and measurements of polydispersity

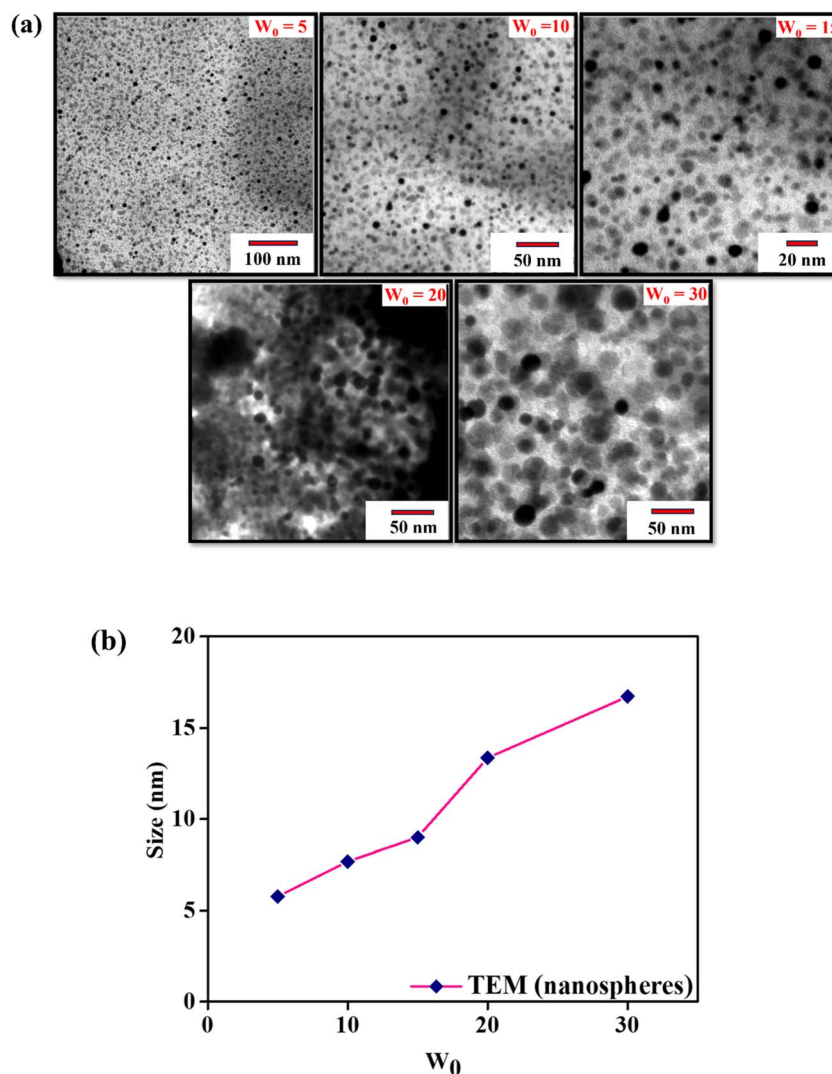


Fig. 2 (a) and (b) show TEM images and the corresponding size analysis, respectively, of FeS nanospheres synthesized from reverse micellar media composed of SPAN 80/1-butanol/toluene/FeS, at different  $W_0$  values.

index (PDI) are employed to carefully examine the impact of  $W_0$  on the synthesised nanoparticles. These three instrumental supports invoked the alterations in surface film rigidity of W/O microemulsions with variations in  $W_0$  values. It is noteworthy that this directly affects the evaluation of targeted nanospheres. Notably, the changes in  $W_0$  have a significant impact on the size as well as surface area of the FeS nanoparticles.

**3.2.1 Analysis of electron microscopic images of FeS.** To more thoroughly investigate the effect of  $W_0$  on FeS nanoparticles, TEM analysis was conducted at 30 °C on the synthesized particles prepared in various microemulsion media with different  $W_0$  values. Fig. 2a depicts the TEM images of nanoparticles, synthesised at various  $W_0$  values (*i.e.* 5, 10, 15, 20 and 30). Furthermore, TEM images confirmed the assessment of nanospheres at various  $W_0$  values used in FeS analysis. At low water content ( $W_0 = 5$ ), the dimensions of the particles determined through TEM microstructural analysis are ranging in between 4.3–8.0 nm (with an average size of 5.7 nm). However, the average size of the nanospheres and the particle size distribution increase gradually as the  $W_0$  value rises (Fig. 2b). For  $W_0 = 10$ , the particles have a size distribution from 6.3 nm to 9.8 nm, with an average diameter of 7.6 nm. By continuing the uphill trend,  $W_0 = 15$  results a mean diameter of 9.0 nm with a particle size distribution of 7.7–10.7 nm. Moreover, conspicuously, at very high-water extent reverse micellar media, the size of synthesized nanospheres is further enlarged to achieve the maximum dimension (as measured through the TEM microstructural analysis). Eventually, at  $W_0 = 20$ , FeS nanospheres have a size range of 10–17 nm (with an average diameter of 13.3 nm) and in a similar fashion, for  $W_0 = 30$ , they are in the range of 13.6–19.3 (with an average diameter of 16.7 nm). Therefore, according to the ongoing microstructural investigations, it is notably concluded that the low water content microemulsions media offered the least dimensional particles. To further reduce the dimensions of the nanospheres,

synthesis at a very low  $W_0$  ( $W_0 = 3$ ) was attempted, but the desired results were not obtained.<sup>43</sup> Therefore, it is thought that  $W_0 = 5$  is the ideal  $W_0$  value to produce appropriate and smaller size nanospheres.

The effect of varying  $W_0$  on the size of the FeS nanostructures are further explored through the FESEM microstructural analysis (as represented in Fig. 3) at 30 °C temperature. FESEM images re-established the evaluations of nanospheres at any  $W_0$  values, employed for FeS synthesis. Furthermore, likewise to the TEM images, this current microscopic study also depicts the gradual raise in the size of the nanospheres to attain the maximum dimension. Therefore, in the arena of current discussions, the least dimensional particle is observed in very low water content media (*i.e.*,  $W_0 = 5$ ). Afterwards, a notable increase in particle size occurs at  $W_0 = 10$  and 15. A faster growth in particle size is noticed whenever the water content ( $W_0 = 10$  and 15) in reverse micellar media is considerably improved. The variation in average diameter (obtained from FESEM microstructural analysis) of FeS nanospheres with different  $W_0$  values is shown in Fig. S3.

**3.2.2 Analysis of polydispersity index (PDI) of colloidal dispersion of FeS nanospheres.** The polydispersity index (PDI) of FeS nanospheres synthesized at different  $W_0$  values was measured to evaluate the influence of water content in reverse micellar systems on particle uniformity. PDI results at various  $W_0$  values are represented in Table 3. Basically, the size distribution of particles, produced from the core of reverse micelle is well-characterized by PDI. A sample exhibiting a perfectly homogeneous particle size distribution has a PDI value of 0.0, whereas a sample with larger particle size distributions and therefore a high degree of polydispersity has a PDI of 1.0.<sup>44</sup>

Table 3 PDI values of spherical FeS nanosphere at different  $W_0$  values

$W_0$ values	5	10	15	20	30
PDI values	0.064	0.111	0.301	0.373	0.786

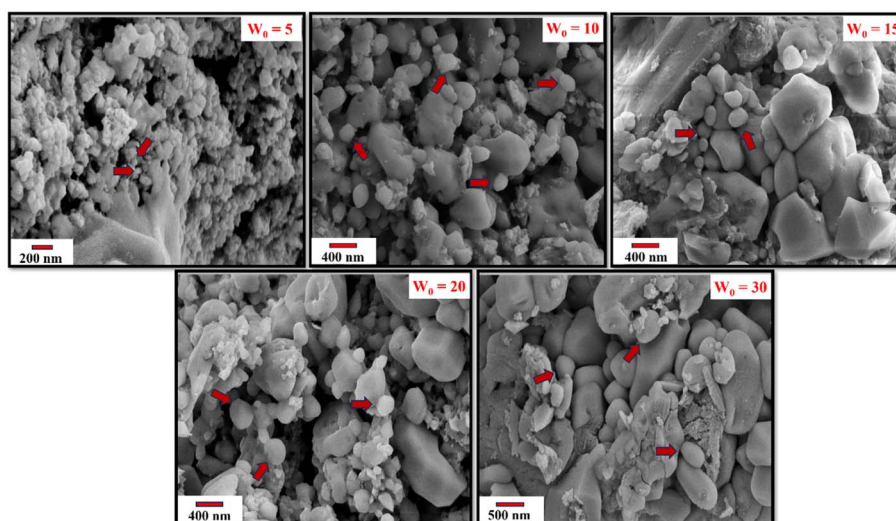


Fig. 3 FESEM images of FeS nanospheres, synthesised from reverse micellar media of SPAN 80/1-butanol/toluene/FeS, at different  $W_0$  values.



Eventually, stated differently, higher the PDI value corresponds to larger the particle size distribution.<sup>43,45</sup>

Agglomeration during reverse micellar synthesis leads to larger, less uniform FeS particles, as evidenced by increased PDI values.<sup>43</sup> It is interesting to note that in the current study, the PDI values for the colloidal dispersion of synthesized FeS are gradually increased by raising the corresponding  $W_0$  values. This implies that from  $W_0 = 5$  to 30, the size distribution as well as average particle diameter are increasing gradually, which is already confirmed by the TEM and FESEM microstructural analysis. More precisely, the produced particles show the lowest PDI value of 0.064 at low water content reverse micellar media ( $W_0 = 5$ ). After that, it went up to 0.111, 0.301 and 0.373 for  $W_0 = 10, 15$  and 20, respectively. Interestingly, at  $W_0 = 30$ , there is a significant increment in the PDI value (having a PDI of 0.786), confirming the maximum agglomeration with the largest average particle diameter. Therefore, by analyzing the results of PDI, it is concluded that the water content in reverse micelle has a great consequence on particle size and corresponding distribution of particles. Moreover, the variation of PDI values of FeS nanospheres at different  $W_0$  values is shown in Fig. S5.

**3.2.3 Assessment of the influence of water-to-surfactant mole ratio ( $W_0$ ).** The water content present within the reverse micellar core, *i.e.*, more precisely the water-to-surfactant mole ratio ( $W_0$ ) intriguingly controlled the size of the evaluated nanoparticles. In the current investigations, several microstructural analyses have invoked the fact that the dimensions of the synthesized FeS nanostructure gradually uplifting the water content raises from  $W_0 = 5$  to 30 (as shown in Fig. 4, through a schematic illustration). Actually, at low water content in reverse micellar media (*i.e.*, more preferably at  $W_0 = 5$  and 10)

surfactant molecules form strong interactions with water molecules located in the hydrophilic core.<sup>43</sup> As a result, the exchange rate between the reverse micelles decreases, which in turn reduces the potential for blending the synthesized particles, causing them to remain in separate reverse micellar cores. Consequently, this causes the targeted particles to stabilise and also gives rise to extremely monodisperse, small-sized nanostructures.<sup>43,45</sup> The PDI value displayed in Table 3 supports this observable monodispersity. Conversely, the intermicellar exchange rate increases as the water content within the polar inner core rises (*i.e.*, for  $W_0 = 15$  and 20). Actually, at high water content reverse micellar media, surfactant molecules are less tightly bound to inner water molecules which pronounced the likelihood of droplet coalescence, interaction, and division.<sup>43</sup> Subsequently, the reactants in different microemulsion media mixed at a higher rate during the nucleation and growth phases. It therefore concludes to be less monodispersed, larger dimensional nanospheres. The advancement of less monodisperse nanospheres is clearly supported by the steady rise in the PDI value (represented in Fig. S5) for  $W_0 = 15$  and 20. In a comparable manner, in very high-water content media ( $W_0 = 30$ ), surfactant molecules are least strongly connected to the polar core, effectively increasing the rate of inter-droplet exchange. Consequently, this leads to the production of least monodisperse, maximum dimensional FeS nanospheres. A few previous studies revealed the following trend concerning the influence of  $W_0$  on the formation of nanoparticles. According to the previous work by Rahaman *et al.*,<sup>15</sup> in contrast to reverse micellar systems with high moisture content ( $W_0 = 50$ ), smaller dimensional lanthanum carbonate nanorods are produced in low moisture content medium ( $W_0 = 10$ ). Similar observations

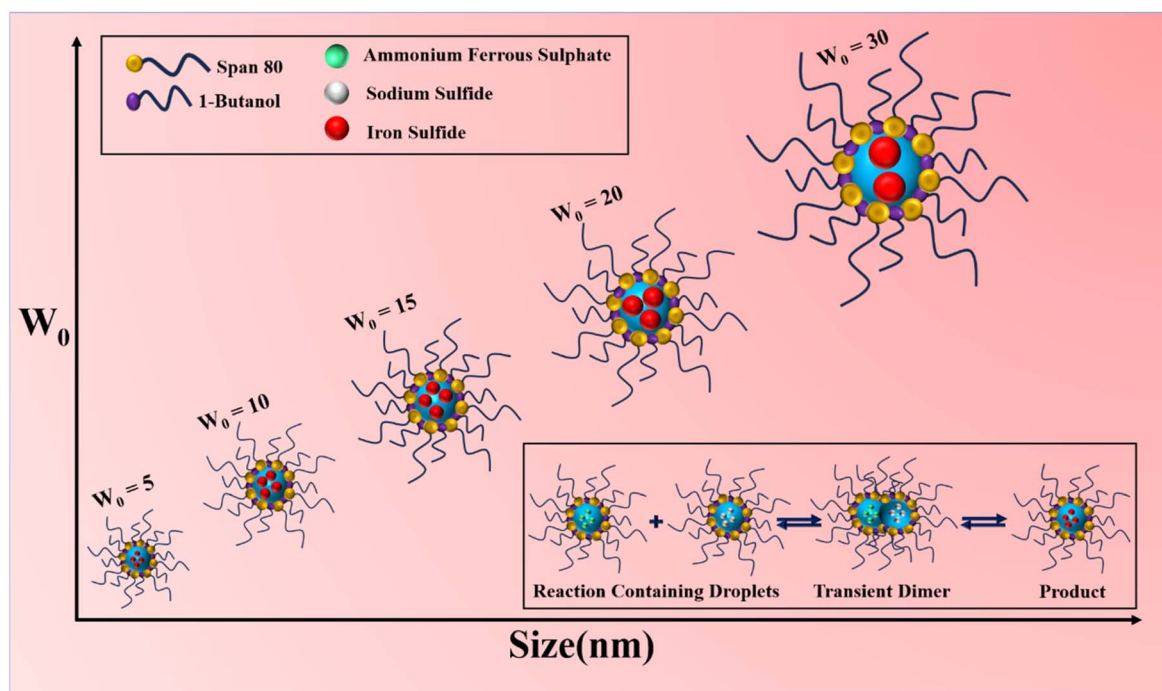


Fig. 4 Schematic representation of the effect of  $W_0$  on the size of evaluated FeS nanospheres.



were identified by Solanki *et al.* during the synthesis of Ag nanoparticles by using different types of reducing agents ( $\text{NaBH}_4$  and  $\text{N}_2\text{H}_4$ ). A consistent increase in particle size is seen for  $W_0 = 3$  to 5 to 8 for both the reducing agents.<sup>43</sup>

### 3.3 Fabrication of Pickering emulsion, stabilised by FeS nanospheres

FeS nanoparticles have a broader area of applications in the modern era. It has a biological application owing to its anti-bacterial and anti-fungal activity.<sup>46,47</sup> However, FeS particles are employed in wastewater treatment and soil remediation.<sup>46,47</sup> This study shows that FeS nanospheres can form Pickering emulsions, a rare use for metal sulfide nanoparticles. The formation of Pickering emulsions by using metal sulfide nanoparticles has been rarely reported. To stabilize the O/W Pickering emulsion, Huang *et al.* hydrophobized lead sulfide nanoparticles using cinnamic acid and oleic acid.<sup>48</sup> In a recent investigation, Rahaman *et al.* utilized lanthanum sulfide nanoparticles (CTAB was used for *in situ* hydrophobization) in pH switchable Pickering emulsion formation.<sup>15</sup> Smaller FeS nanospheres have higher surface area and readily adsorb at the toluene–water interface, separating the non-polar and polar phases.<sup>15</sup> At low water content (*i.e.*,  $W_0 = 5$ ),  $\sim 5.7$  nm

nanospheres are formed and were thus used for Pickering emulsion stabilization. The stability of the Pickering emulsion, stabilised by FeS nanosphere at different  $W_0$  are further experimentally analysed by measuring the average diameter of the emulsion droplets (shown in Fig. S6). From the inspection of Fig. 5a, it is clearly concluded that the diameter of these droplets is significantly influenced by the size of the nanospheres, synthesised from different  $W_0$  values. At higher values of  $W_0$  (*i.e.*  $W_0 = 20$  and 30) the resulting emulsion droplets are larger in size and failed to attain the desired stability. Interestingly, as the  $W_0$  value is gradually reduced to  $W_0 = 5$ , a notable reduction in droplet diameter is observed, suggesting an enhancement in the stability of the Pickering emulsion.

To prepare the Pickering emulsion, FeS nanoparticles synthesized from a W/O microemulsion medium (with  $W_0 = 5$ ) are used at varying wt% (0.0125, 0.025, 0.05, and 0.075), along with 2 mL of water as the aqueous phase and 2 mL of toluene as the oil phase. All of the above-mentioned sets are homogenised to prepare the Pickering emulsion and then digital images (Fig. S4) as well as optical micrographs (Fig. S7) of the so-prepared emulsion droplets are taken after 1 h of standings. The dilution method demonstrated the O/W nature of the Pickering emulsion, as droplets dispersed in water but not in

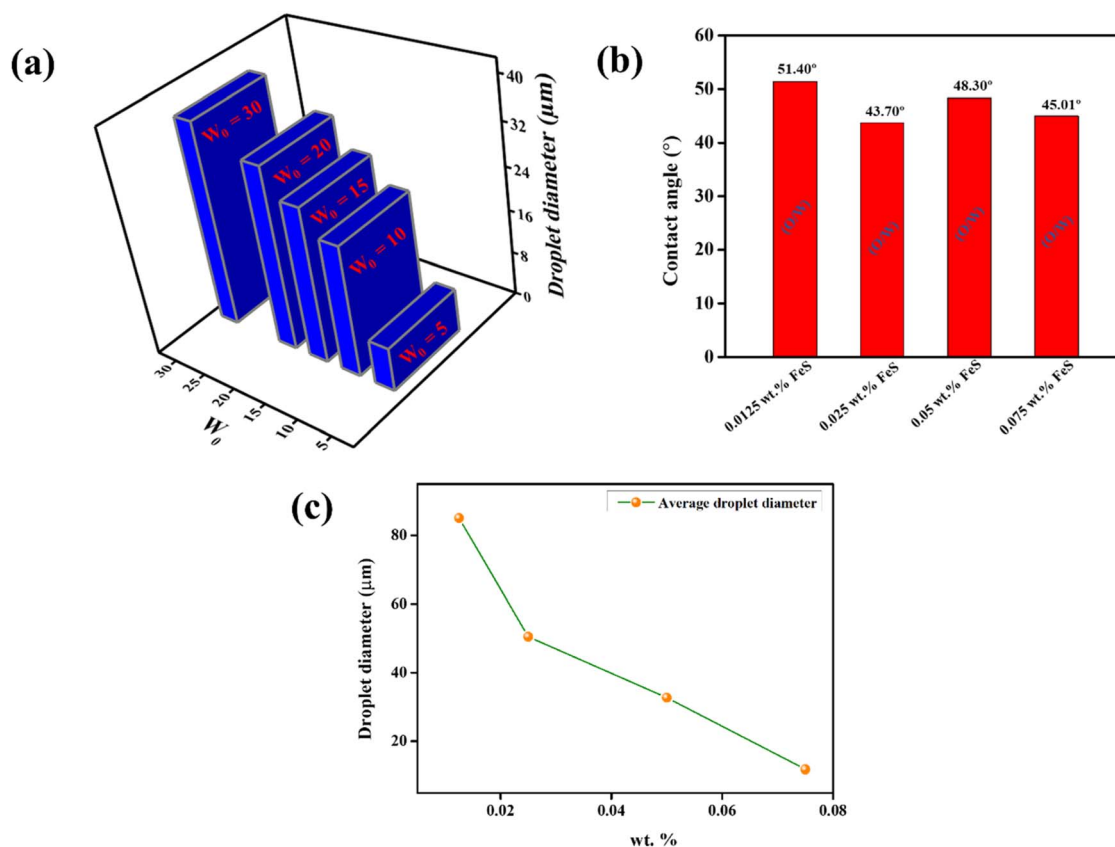


Fig. 5 (a) Variation in the average droplet diameter (measured after 1 hour of standing) of Pickering emulsions stabilized by FeS nanospheres (at a fixed concentration of 0.075 wt%), synthesized in reverse micellar media with different  $W_0$ , (b) contact angle of Pickering emulsions stabilized by varying concentrations of FeS nanospheres, synthesized at  $W_0 = 5$ , and (c) variation in the mean droplet diameter (measured after 1 hour of standing) of Pickering emulsions formed using different concentrations of FeS nanospheres, synthesized from reverse micellar media with  $W_0 = 5$ .



toluene.<sup>15,49,50</sup> Nature of the emulsion can be predicted *via* the analysis of contact angle measurement (shown in Fig. 5b). Generally lower contact angle value ( $<90^\circ$ ) suggests the formation of O/W type emulsion. In this current study, the contact angle at every wt% of FeS nanospheres results at around  $45^\circ$  and thereby confirms the development of O/W type Pickering emulsions.<sup>51</sup>

The average diameter of the emulsion droplets is measured in order to analyse the stability of the Pickering emulsion and droplets diameter, in its turn strongly reliant on the wt% of the nanospheres present in the polar phase. At relatively low concentrations (0.0125 and 0.025 wt%) of nanospheres, the produced emulsion droplets are larger in size and are unable to achieve the desired stability. When the nanosphere content is progressively increased to 0.075 wt%, the droplet diameter decreases noticeably (Fig. 5c), indicating the enhanced stability of the Pickering emulsion. At 0.0125 and 0.025 wt% of nanospheres, the Pickering emulsion exhibits complete separation of phases, with droplet sizes of 83  $\mu\text{m}$  and 50  $\mu\text{m}$  on average, respectively. In contrast, the Pickering emulsion at 0.05 and 0.075 wt% of nanospheres shows no noticeable change in droplet size. At elevated nanosphere concentrations, the fabricated particles efficiently adsorb to the oil–water boundary, enclosing the oil phase and separating it from the aqueous phase. This reduces the possibility of coalescing emulsion droplets and eventually provides a distinct interface between the two phases.<sup>15,52</sup> It therefore results in the formation of more stable, smaller size emulsion droplets at comparatively very high wt% of nanospheres. Consequently, a Pickering emulsion stabilized by 0.075 wt% of nanospheres is utilized as a highly efficient template for the further polymerization of aniline.

The impact of varying the wt% of nanosphere on the stability of Pickering emulsions is further validated by assessing the viscosity of the emulsion system. As seen in Fig. 6 the viscosity–shear rate plots exhibit notable shear-thinning behaviour in the Pickering emulsion at different wt% of the synthesized

nanosphere. The shear-thinning behaviour suggests the persistence of a network structure, which is probably due to the interactions between droplets in the Pickering emulsions.<sup>53</sup> As the shear rate increases, the viscosity of all the emulsified systems decreases steadily, and thereafter stabilizing at higher shear rates.<sup>16,53</sup> Over the complete shear stress range, the Pickering emulsion containing 0.05 wt% of FeS nanosphere demonstrates higher viscosity than the emulsion with 0.025 wt% of FeS nanosphere. Additionally, nanosphere containing 0.075 wt% of FeS provided further improvements in the viscosity of the examined Pickering emulsion. This behaviour suggests that the droplets at the toluene–water interface become more tightly packed by uplifting the wt% of FeS nanosphere, leading to increased viscosity and ultimately inhibiting inter-droplet coalescence.<sup>16</sup> The formation of a stable emulsified system at higher FeS wt% (0.05 or 0.075) can be attributed to the presence of smaller and more uniform droplets. The robust network formation between the droplets results in the system exhibiting a creamy appearance (Fig. S4). In contrast, at low FeS concentrations (0.0125 wt%), the emulsion droplet size increases due to rapid coalescence, ultimately leading to phase separation into two transparent layers, lacking a creamy appearance. The varying viscosity behaviour with respect to FeS wt% facilitates the utilisation of 0.075 wt% of nanospheres in Pickering emulsion-based polymerisation of aniline to form FeS@PANI.

### 3.4 Characterisation of FeS@PANI nanocomposites

The before mentioned stable Pickering emulsions (incorporating 0.075 wt% of nanospheres for stabilization) are employed as a scaffold for the polymerisation of aniline to synthesize the FeS@PANI nanostructured composites. Leveraging this well-dispersed emulsion stabilized by nanoparticles, the polymerization of aniline at the oil–water boundary was activated by adding potassium persulfate as an oxidant. When an oxidant is added, the Pickering emulsion slowly changes to dark green, providing a definitive indication of the formation of FeS@PANI nanocomposites.<sup>40</sup> By adding oxidant directly to the aniline, a blank study was also conducted to compare the effects of utilising Pickering emulsion against not using it. The synthesised nanocomposites were supported by PXRD, UV, IR, and  $^1\text{H}$  NMR instrumental investigations. TEM and FESEM microstructural analysis were further carried out to investigate the effect of employed FeS nanospheres on the size and morphology of FeS@PANI nanocomposites.

**3.4.1 Analysis of PXRD data.** Fig. 7a illustrates the powder X-ray diffraction (XRD) patterns of the synthesized samples. In addition to the broad characteristic peak of PANI at  $2\theta = 25.53^\circ$ , a distinct peak at  $2\theta = 28.15^\circ$  is also observed for PANI, suggesting the successful polymerization of aniline *via* Pickering emulsion method.<sup>54,55</sup> Moreover, the PXRD analysis also confirms the successful synthesis of the targeted FeS@PANI polymeric nanocomposites through the detection of characteristic peaks of FeS along with the above-mentioned peaks of PANI. It therefore clears evidence of effective incorporation of FeS into the polymeric matrix. Interestingly, the FeS@PANI

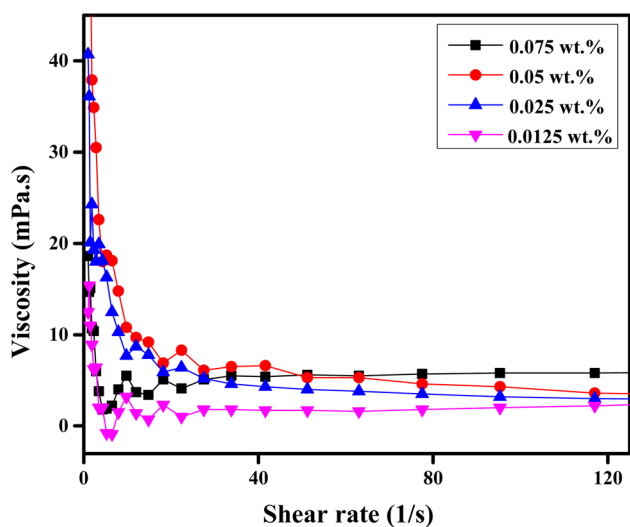


Fig. 6 Viscosity of the Pickering emulsion, stabilized by varying wt% of FeS nanospheres, synthesised from  $W_0 = 5$ .

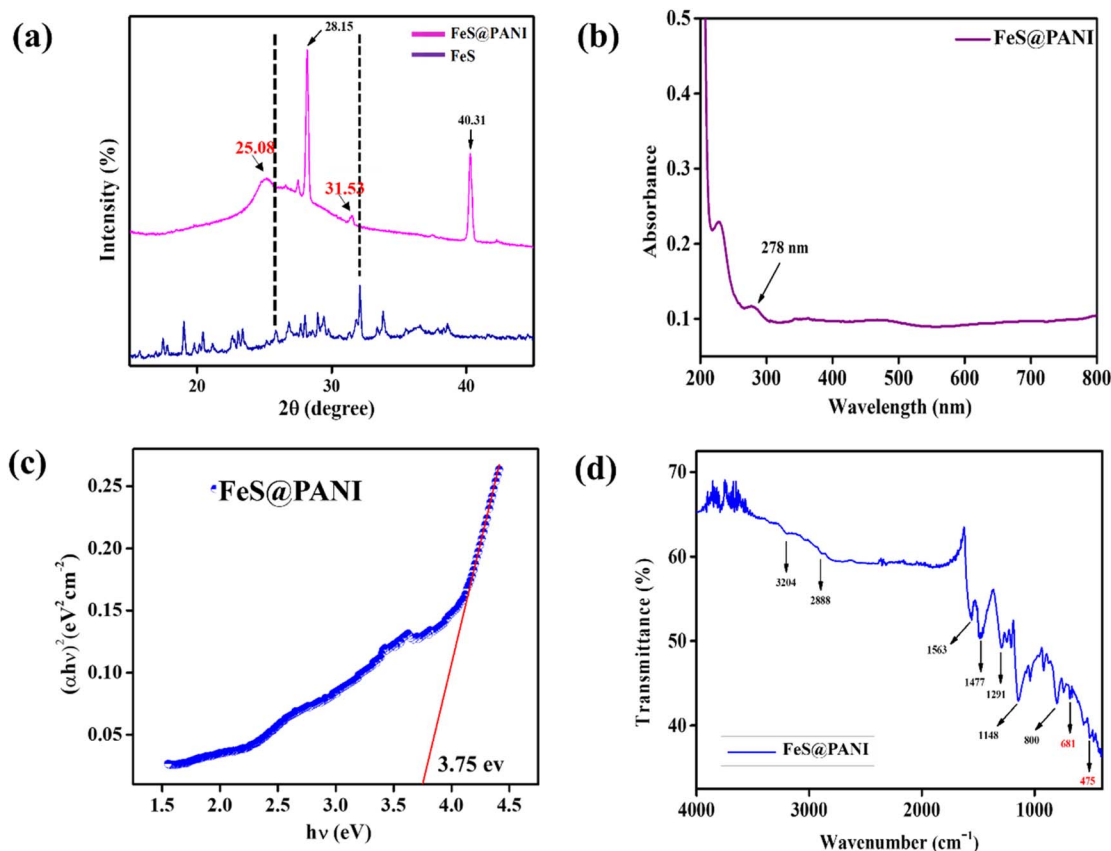


Fig. 7 (a) A comparative PXRD spectral analysis of FeS@PANI nanocomposites and FeS nanoparticle, (b) UV-Vis absorption data, (c) energy band gap determination plot, and (d) FTIR spectrum of FeS@PANI nanocomposites.

composite exhibits slight shifts in peak positions and intensities compared to pure FeS, which can be attributed to the low FeS content. Specifically, the PXRD peaks of pure FeS at  $2\theta = 25.90^\circ$  and  $32.02^\circ$  are shifted to  $2\theta = 25.08^\circ$  and  $31.53^\circ$ , respectively, in the composite, corresponding to shifts of  $0.82^\circ$  and  $0.49^\circ$  toward lower angles.<sup>56</sup> These shifts further support the presence of interactions between FeS and PANI within the composite structure.

**3.4.2 UV-visible analysis and calculation of optical band gap ( $E_g$ ).** Analysing the spectroscopic characteristics of the FeS@PANI composite is a crucial step in investigating the possible uses of reverse micellar-templated FeS nanospheres. The UV-visible absorption spectra of the composite FeS@PANI are presented in Fig. 7b. The  $\pi$ - $\pi^*$  and polaron- $\pi^*$  transitions of the conducting PANI are responsible for the majority of the optical absorption, which has been identified to be 278 nm for the synthesised composite.<sup>57,58</sup> However, PANI typically shows a distinct peak around 300 nm, and the observed shift in FeS@PANI nanocomposites can be attributed to the complexation of PANI with FeS nanospheres.<sup>57,58</sup>

The optical band gap,  $E_g$ , can be determined *via* the absorption coefficient ( $\alpha$ ), which can be calculated as a function of incident photon energy,  $h\nu$ .<sup>57,58</sup> Generally, the reaction is represented as follows:

$$\alpha h\nu = B(h\nu - E_g)^m \quad (1)$$

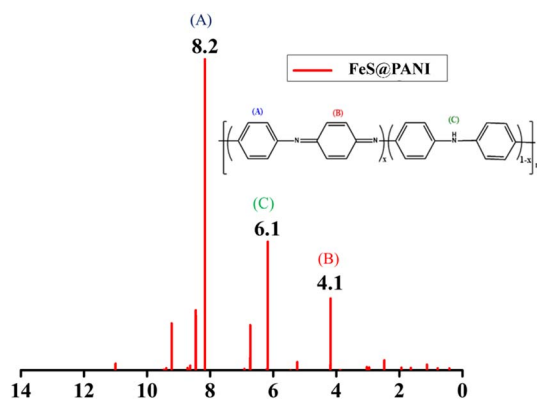
here,  $\alpha$  represents the absorption coefficient,  $h$  represents the Planck constant,  $\nu$  stands for the incident light frequency,  $E_g$  corresponds to the energy band gap of the nanocomposites, and  $m$  indicates the type of transition (direct or indirect). The electronic transition gap values for FeS@PANI are obtained by extrapolating the linear segment of the  $(\alpha h\nu)^2$  versus  $h\nu$  curve to the point where  $\alpha h\nu = 0$ . As depicted in Fig. 7c, the value for the FeS@PANI nanocomposites is determined to be 3.75 eV. The outcomes exhibit a striking resemblance to those reported by Sasikumar *et al.* using PANI@TiO<sub>2</sub> nanocomposites.<sup>57</sup> Similar findings regarding the band gap of the PANI@Sm<sub>2</sub>S<sub>3</sub> nanocomposites were reported by Rahaman *et al.*, who synthesized them using the Pickering emulsion polymerization process.<sup>15</sup> In terms of enhanced conductivity and stimulated carrier production, this small band-gap would be more beneficial.

**3.4.3 Analysis of FTIR spectrum.** The FTIR spectrum of FeS@PANI nanocomposites is depicted in Fig. 7d. In contrast to the spectrum of pure FeS nanospheres, the FTIR spectra of FeS@PANI reveal additional peaks at 800, 1148, 1291, 1477, 1563, 2888, and 3204 cm<sup>-1</sup>, which are characteristic of polyaniline.<sup>57-60</sup> Furthermore, the two pure peaks of FeS at 611 and 414 cm<sup>-1</sup> (as represented in Fig. 1b) are considerably shifted to 681 and 475 cm<sup>-1</sup> as a result of the complexation of FeS nanospheres and synthesised PANI.<sup>46,57-59</sup> As a result, the information provided above clearly demonstrates the



**Table 4** The appropriate assignment with their corresponding primary band position of FeS@PANI nanocomposites in the FTIR spectrum

Band position (cm <sup>-1</sup> ) of FeS@PANI	Assignment
800	<i>Para</i> substituted
1148	Benzenoid rings
1291	C–N stretching
1477	C=C stretching (aromatic ring)
1563	Quinoid rings
2889	C–H stretching (aromatic ring)
3204	N–H stretching

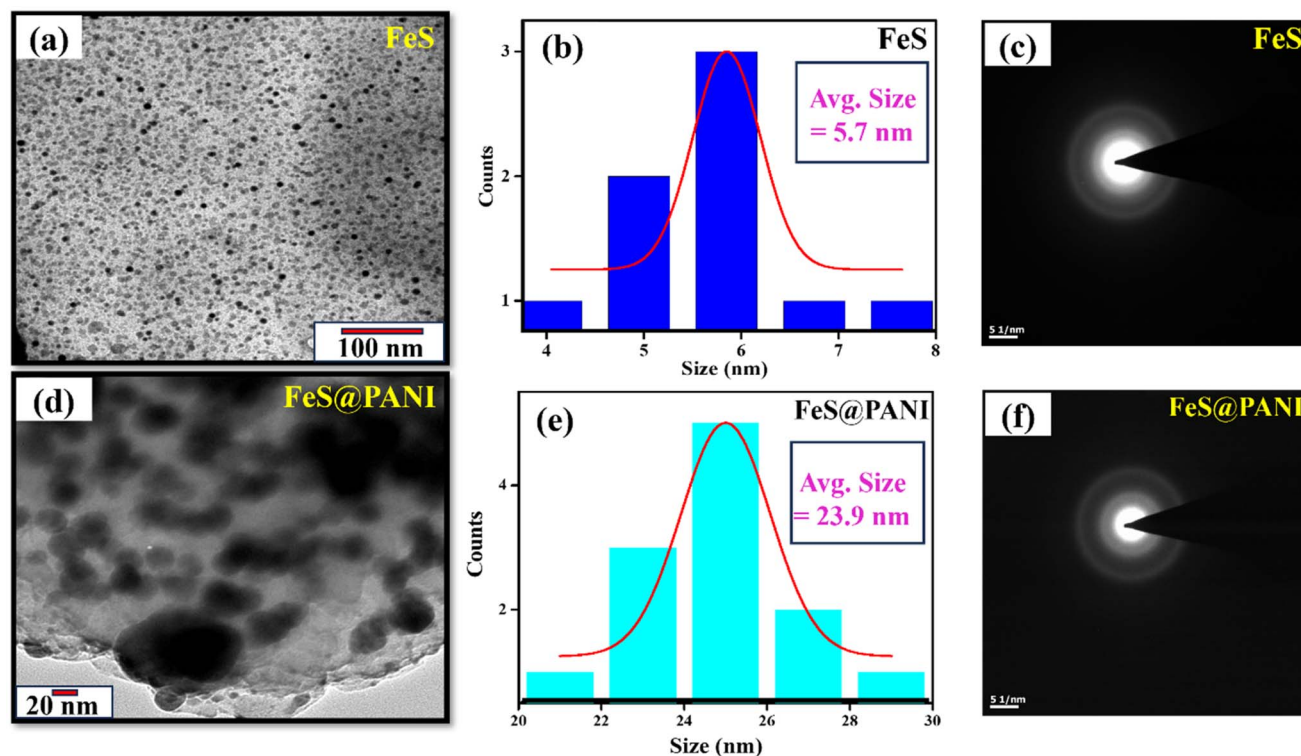
**Fig. 8** <sup>1</sup>H-NMR analysis of FeS@PANI nanocomposites in CDCl<sub>3</sub> solvent.

persistence of PANI and the successful formation of FeS@PANI nanocomposites through Pickering emulsion mediation. Additionally, the FTIR findings align well with the existing literature on PANI. Table 4 displays the distributions of all the key absorption bands (in the FTIR spectra) for the nanocomposites, which have been previously identified.

**3.4.4 Interpretation of the <sup>1</sup>H-NMR spectrum of FeS@PANI nanocomposites.** Analysis of the <sup>1</sup>H-NMR spectrum reveals information about the signals from the different types of protons in the FeS@PANI nanocomposites. Fig. 8 displays the <sup>1</sup>H-NMR spectra of the nanocomposites (in CDCl<sub>3</sub> solvent). An intense peak of about 8.2 ppm is produced due to the presence of aromatic protons (A) in FeS@PANI nanocomposites.<sup>59,60</sup> Furthermore, a peak at 6.1 ppm is apparent, attributed to the benzenoid rings (C) in the composites.<sup>59,60</sup> Additionally, a peak around 4.1 ppm is observed, corresponding to the *para* position on aniline (B) used in the polymerization reaction.

**3.4.5 TEM microstructural analysis of FeS@PANI nanocomposites.** Fig. 9a and d shows the TEM images of the synthesized FeS nanoparticle and FeS@PANI nanocomposites. Microstructural analysis suggests the formation of spherical polymeric particles within the nonpolar scaffolds of oil–water Pickering emulsions, along with the presence of spherical nanocomposites. These spherical polymeric structures are interconnected, indicating the formation of a polymeric chain, consistent with previous observations.<sup>61,62</sup>

The average size of the FeS@PANI nanocomposites is approximately 23.9 nm, which is larger than the size of the FeS

**Fig. 9** (a) and (d) TEM images, (b) and (e) particle size distribution histograms, (c) and (f) SAED patterns of FeS nanoparticles and FeS@PANI nanocomposites, respectively.



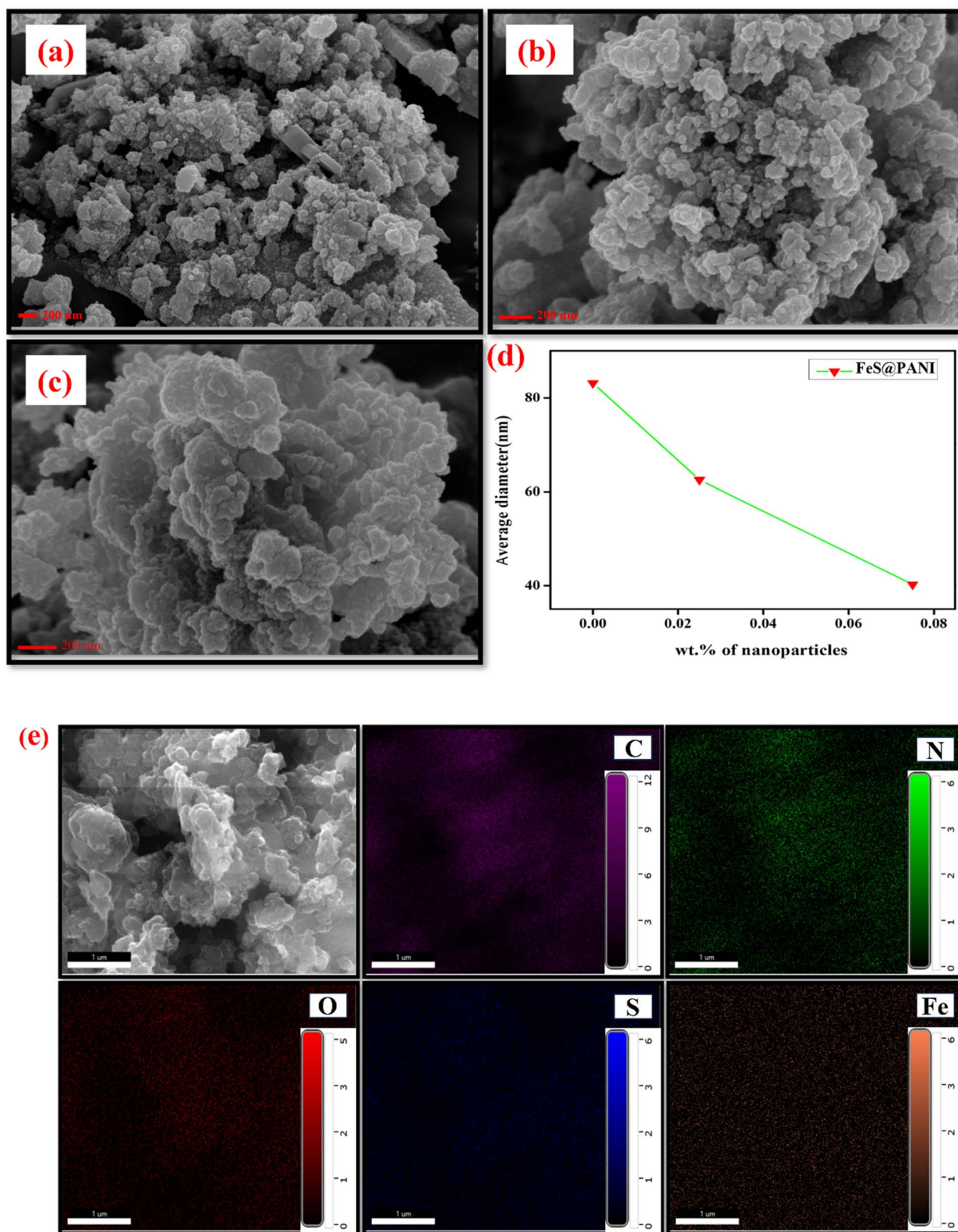


Fig. 10 FESEM images of FeS@PANI nanocomposites having different wt% of FeS in polar phase (a) 0.075, (b) 0.025 and (c) 0. (d) Variation of average diameter of FeS@PANI nanocomposites by varying the wt% of FeS nanospheres; (e) elemental mapping image of FeS@PANI nanocomposites.



nanoparticles (5.7 nm, synthesized at  $W_0 = 5$ ) (Fig. 9b and e). This increase in size clearly suggests the formation of FeS@PANI through interactions between FeS nanoparticles and polymerized aniline.

The SAED (Selected Area Electron Diffraction) patterns for both FeS and FeS@PANI are also shown in Fig. 9c and f respectively. SAED is commonly used to distinguish between powdered and crystalline samples by examining their diffraction patterns: crystalline samples exhibit sharp, discrete diffraction spots, while powdered samples show ring-like patterns. In this case, both FeS and FeS@PANI display ring patterns, confirming their powder-like nature.

Moreover, the similarity of the SAED patterns before and after polymerization indicates that the crystalline phase of the FeS nanoparticles remains unchanged. Therefore, both FeS and FeS@PANI can be classified as powder-phase materials.

**3.4.6 FESEM microstructural analysis of FeS@PANI nanocomposites.** It is observed that the amount of nanospheres used in the dispersion affects the size and morphology of spherical shape FeS@PANI nanocomposites. Fig. 10 displays the FESEM images of FeS@PANI composites having various wt% FeS nanospheres. FESEM images of polyaniline, when nanospheres are absent, show agglomerated nanostructures with an average size of 83 nm, revealing notable distortion in their spherical structure (Fig. 10c). In contrast, the size and shape of the targeted polyaniline are expertly designed with the inclusion of FeS stabilised Pickering emulsion. The scaffold of the emulsion droplets functions as a framework for the polymerization process.<sup>39,40</sup> Wang *et al.* previously reported the synthesis of polyaniline@MnO<sub>2</sub>/graphene ternary hybrid hollow spheres *via* Pickering emulsion polymerization, where MnO<sub>2</sub>-coated graphene was used as the stabilizer to ensure the stability of the Pickering emulsion composed of toluene and water.<sup>24</sup> A closer look at Fig. S7 reveals that the rigidity of the surface film of the emulsion droplets was pronounced as the wt% (0 to 0.075 wt%) of FeS nanospheres were progressively raised, resulting in a decrease in the droplet diameter. Generally, by increasing the wt% of FeS, it efficiently placed into the interface of toluene-water and thereby decreased the probability of agglomeration, leading to the evaluation of spherically distributed FeS@PANI nanocomposites with gradual reduction of particle size (for 0.025 wt%: 62 nm and 0.075 wt%: 40 nm). Since PANI is a promising conducting polymer, from a future perspective, these so-produced PANI-based nanocomposites have the potential for diverse applications in various fields.<sup>39,40</sup>

The successful synthesis of FeS@PANI nanocomposites was further validated through complementary characterization techniques, including energy-dispersive X-ray spectroscopy (EDX) and elemental mapping, in addition to PXRD, FTIR and <sup>1</sup>H-NMR analyses. Fig. 10e displays the elemental mapping of the FeS@PANI nanocomposites, clearly showing the uniform presence of key elements carbon (C), nitrogen (N), oxygen (O), sulfur (S), and iron (Fe) across the sample. These elemental analyses correspond to the expected composition of the FeS core and the polyaniline shell. Quantitative elemental data obtained from EDX analysis are summarized in Table S1 of the SI. The spatially homogeneous distribution of these elements

provides strong evidence for the successful encapsulation of FeS nanoparticles within the polyaniline matrix, thereby confirming the effectiveness of the Pickering emulsion polymerization approach used in the synthesis.

## 4. Conclusion

In this study, reverse micelle-mediated FeS nanospheres were synthesized and employed as stabilizers in Pickering emulsion polymerization to fabricate FeS@PANI nanocomposites. The water-to-surfactant molar ratio ( $W_0$ ) significantly influenced nanosphere size and morphology, with values ranging from 5 to 30 in a system consisting of toluene, SPAN 80, 1-butanol, and FeS. TEM and FESEM microstructural analysis, along with PDI evaluations, confirmed that increasing the water content from  $W_0 = 5$  to  $W_0 = 30$  led to a progressive increase in the nanosphere size. Lower  $W_0$  (*i.e.*,  $W_0 = 5$ ) led to smaller, monodisperse particles due to strong surfactant-water interactions and limited intermicellar exchange. In contrast, higher  $W_0$  (*i.e.*,  $W_0 = 30$ ) values resulted in larger, less uniform nanospheres due to enhanced inter-droplet exchange.

FeS nanospheres synthesized at  $W_0 = 5$  formed stable O/W Pickering emulsions, with optimal stability achieved at 0.075 wt% FeS. These emulsions exhibited compact droplet structures and high resistance to coalescence, supported by viscosity measurements. Using these emulsions, FeS@PANI nanocomposites were synthesized and confirmed *via* PXRD, UV-Vis, IR, and <sup>1</sup>H-NMR analyses.

The FeS concentration directly influenced nanocomposite morphology. At 0.075 wt%, well-defined spherical particles (~40 nm) were obtained, while reduced FeS content (0.025 wt%) led to larger (~62 nm) structures. In the absence of FeS, only aggregated, poorly defined particles formed. This study highlights the dual function of FeS nanospheres as effective emulsion stabilizers and morphology-directing agents in the synthesis of high-performance polymer nanocomposites, offering a versatile platform for designing advanced materials with tunable properties for diverse applications.

## Conflicts of interest

There are no conflicts to declare.

## Data availability

Data will be made available on request.

Supplementary information (SI): contains the data of Optical Microscope and Field Emission Scanning Electron Microscope. See DOI: <https://doi.org/10.1039/d5ra03785a>.

## Acknowledgements

N. K. acknowledges Govt. of West Bengal for providing the Swami Vivekananda Merit Cum Means Scholarship (SVMCM).

## References

- 1 G. Verma, K. Mondal, M. Islam and A. Gupta, *ACS Appl. Eng. Mater.*, 2024, **2**, 262–285.
- 2 D. M. Alshangiti, T. K. El-damhougy, A. Zaher, M. Madani and M. Mohamady ghobashy, *RSC Adv.*, 2023, **13**, 35251–35291.
- 3 N. Baig, I. Kammakakam and W. Falath, *Mater. Adv.*, 2021, **2**, 1821–1871.
- 4 A. Kumar, S. Dutta, S. Kim, T. Kwon, S. S. Patil, N. Kumari, S. Jeevanandham and I. S. Lee, *Chem. Rev.*, 2022, **122**(15), 12748–12863.
- 5 N. M. Correa, J. J. Silber, R. E. Riter and N. E. Levinger, *Chem. Rev.*, 2012, **112**(8), 4569–4602.
- 6 S. N. Mohamad-Aziz, A. W. Zularisam and A. M. M. Sakinah, *Sep. Purif. Technol.*, 2019, **229**, 115816.
- 7 R. G. Chaudhuri and S. Paria, *Chem. Rev.*, 2012, **112**(4), 2373–2433.
- 8 S. Chandrasekaran, L. Yao, L. Deng, C. Bowen, Y. Zhang, S. Chen, Z. Lin, F. Peng and P. Zhang, *Chem. Soc. Rev.*, 2019, **48**, 4178–4280.
- 9 F. Jamal, A. Rafique, S. Moeen, J. Haider, W. Nabgan, A. Haider, M. Imran, G. Nazir, M. Alhassan, M. Ikram, Q. Khan, G. Ali, M. Khan, W. Ahmad and M. Maqbool, *ACS Appl. Nano Mater.*, 2023, **6**(9), 7077–7106.
- 10 D. G. Ortiz, C. Pochat-Bohatier, J. Cambedouzou, M. Bechelany and P. Miele, *Eng.*, 2020, **6**, 468–482.
- 11 M. Xu, W. Zhang, J. Jiang, X. Pei, H. Zhu, Z. Cui and B. P. Binks, *Langmuir*, 2020, **36**, 15543–15551.
- 12 S. Lam, K. P. Velikov and O. D. Velev, *Curr. Opin. Colloid Interface Sci.*, 2014, **19**, 490–500.
- 13 S. Yu, H. Zhang, J. Jiang, Z. Cui, W. Xia and B. P. Binks, *Green Chem.*, 2020, **22**, 5470–5475.
- 14 P. Zhu, F. Wang, Y. Ding, S. Zhang, C. Gao, P. Liu and M. Yang, *Langmuir*, 2021, **37**, 4082–4090.
- 15 S. M. Rahaman, M. Chakraborty, T. Mandal, N. Khatun, A. Patra, M. Chakravarty and B. Saha, *J. Mol. Liq.*, 2024, **413**, 125904.
- 16 T. Mandal, S. M. Rahaman, B. Saha, N. Khatun, A. Patra, A. Mukherjee, M. Nandi, D. Dhak, S. Roy and B. Saha, *New J. Chem.*, 2024, **48**(22), 10112–10125.
- 17 Y. Zhu, T. Fu, K. Liu, Q. Lin, X. Pei, J. Jiang, Z. Cui and B. P. Binks, *Langmuir*, 2017, **33**, 5724–5733.
- 18 P. A. Demina, D. V. Voronin, E. V. Lengert, A. M. Abramova, V. S. Atkin, B. V. Nabatov, A. P. Semenov, D. G. Shchukin and T. V. Bukreeva, *ACS Omega*, 2020, **5**, 4115–4124.
- 19 N. Fessi, M. F. Nsib, Y. Chevalier, C. Guillard, F. Dappozze, A. Houas, L. Palmisano and F. Parrino, *Langmuir*, 2019, **35**, 2129–2136.
- 20 M. Giménez-Marqués, T. Hidalgo, C. Serre and P. Horcajada, *Coord. Chem. Rev.*, 2016, **307**, 342–360.
- 21 T. Zhang, R. A. Sanguramath and S. Israel, *Macromolecules*, 2019, **52**, 5445–5479.
- 22 M. N. A. Said, N. A. Hasbullah, M. R. H. Rosdi, M. S. Musa, A. Rusli and A. Ariffin, *ACS Omega*, 2022, **7**, 47490–47503.
- 23 J. N. Kim, Y. Z. Dong and H. J. Choi, *ACS Omega*, 2020, **5**, 7675–7682.
- 24 Y. Wang, B. Hu, J. Luo, Y. Gu and X. Liu, *ACS Appl. Eng. Mater.*, 2021, **4**, 7721–7730.
- 25 T. H. Qazi, R. Rai and A. R. Boccaccini, *Biomaterials*, 2014, **35**, 9068–9086.
- 26 E. Bourgeat-Lami, G. A. Farzi, L. David, J.-L. Putaux and T. F. L. McKenna, *Langmuir*, 2012, **28**(14), 6021–6031.
- 27 B. Kaur, G. Kaur, G. R. Chaudhary, V. K. Sharma, H. Srinivasan, S. Mitra, A. Sharma, S. L. Gawali and P. A. Hassan, *J. Mol. Liq.*, 2020, **318**, 114034.
- 28 J. Arjomandi, J. Y. Lee, R. Movafagh, H. Moghanni-Bavil-Olyaei and M. H. Parvin, *J. Electroanal. Chem.*, 2018, **810**, 100–108.
- 29 S. Konwer, A. K. Guha and S. K. Dolui, *J. Mater. Sci.*, 2013, **48**(4), 1729–1739.
- 30 P. Bera, R. V. Lakshmi, R. P. S. Chakradhar, S. Bose and H. C. Barshilia, *Funct. Compos. Mater.*, 2024, **5**, 11.
- 31 B. L. Cushing, V. L. Kolesnichenko and C. J. O'Connor, *Chem. Rev.*, 2004, **104**, 3893–3946.
- 32 D. S. Mathew and R.-S. Juang, *J. Chem. Eng.*, 2007, **129**, 51–65.
- 33 D. Li, B. Gao and X. Cui, *New J. Chem.*, 2022, **46**, 16858–16873.
- 34 P. M. Sy, N. Anton, Y. Idoux-Gillet, S. M. Dieng, N. Messaddeq, S. Ennahar, M. Diarra and T. F. Vandamme, *Int. J. Pharm.*, 2018, **549**, 299–305.
- 35 H. Zhu, W. Luo, P. N. Ciesielski, Z. Fang, J. Y. Zhu, G. Henriksson, M. E. Himmel and L. Hu, *Chem. Rev.*, 2016, **116**, 9305–9374.
- 36 C.-H. Cui and S.-H. Yu, *Acc. Chem. Res.*, 2013, **46**, 1427–1437.
- 37 Y. Wu, X. Zhao, Y. Shang, S. Chang, L. Dai and A. Cao, *ACS Nano*, 2021, **15**, 7946–7974.
- 38 Z. Cai, Y. Wei, A. Shi, J. Zhong, P. Rao, Q. Wang and H. Zhang, *Adv. Colloid Interface Sci.*, 2023, **313**, 102863.
- 39 H. Asoufi, T. M. Al-Antary and A. Awwad, *Fresenius Environ. Bull.*, 2018, **27**, 7767–7775.
- 40 T. J. Malek, S. H. Chaki and M. P. Deshpande, *Phys. B*, 2018, **546**, 59–66.
- 41 M. Salavati-Niasari, G. Hosseinzadeh and F. Davar, *J. Alloys Compd.*, 2011, **509**, 134–1401.
- 42 E. G. Il, A. S. Parshakov, L. D. Iskhakova, L. V. Goeva, E. G. Tarakanova, N. P. Simonenko, V. I. Privalov and J. Fluor, *Chem*, 2020, **236**, 109576.
- 43 J. N. Solanki and Z. V. P. Murthy, *Ind. Eng. Chem. Res.*, 2011, **50**(12), 7338–7344.
- 44 M. Danaei, M. Dehghankhold, S. Ataei, F. Hasanazadeh Davarani, R. Javanmard, A. Dokhani, S. Khorasani and M. R. Mozafari, *Pharmaceutics*, 2018, **10**(2), 57.
- 45 C. Petit, P. Lixon and M. P. Pileni, *J. Phys. Chem.*, 1993, **97**(49), 12974–12983.
- 46 E.-J. Kim, J.-H. Kim, A.-M. Azad and Y.-S. Chang, *ACS Appl. Mater. Interfaces*, 2011, **3**(5), 1457–1462.
- 47 S. Bhattacharjee, F. Habib, N. Darwish and A. Shanableh, *Powder Technol.*, 2021, **380**, 219–228.
- 48 Z. Huang, J. T. Koubek, A. Sellinger and M. C. Beard, *ACS Appl. Nano Mater.*, 2022, **5**(3), 3183–3187.





- 49 B. Saha, M. Das, R. K. Mohanty and A. K. Das, *J. Chin. Chem. Soc.*, 2004, **51**(2), 399–408.
- 50 L. Liu, X. Pu, Y. Zhou, X. Wu, D. Luo and Z. E. Ren, *Energy Fuels*, 2020, **34**(2), 1317–1328.
- 51 P. Zhu, F. Wang, Y. Ding, S. Zhang, C. Gao, P. Liu and M. Yang, *Langmuir*, 2021, **37**(14), 4082–4090.
- 52 T. Zeng, A. Deng, D. Yang, H. Li, C. Qi and Y. Gao, *Langmuir*, 2019, **35**(36), 11872–11880.
- 53 S. M. Rahaman, D. Joshi, A. Patra, T. Mandal, N. Khatun, S. Dhibar, R. Saha, A. Mandal, D. Kumar and B. Saha, *New J. Chem.*, 2024, **48**(9), 4063–4076.
- 54 S. Sathiyarayanan, S. Syed Azim and G. Venkatachari, *Synth. Met.*, 2007, **157**, 18–20.
- 55 S. M. Ambalagi, M. Devendrappa, S. Nagaraja and B. Sannakki, *IOP Conf. Ser.: Mater. Sci. Eng.*, 2018, **310**, 012081.
- 56 Y.-F. Wang, D.-L. Liu, J.-J. Han and A.-R. Guo, *Ionics*, 2022, **28**, 2457–2468.
- 57 M. Sasikumar and N. P. Subiramaniam, *J. Mater. Sci.: Mater. Electron.*, 2018, **29**(9), 7099–7106.
- 58 M. Shaban, M. Rabia, W. Fathallah, N. A. El-Mawgoud, A. Mahmoud, H. Hussien and O. Said, *J. Polym. Environ.*, 2018, **26**(2), 434–442.
- 59 N. K. Jangid, N. P. S. Chauhan and P. B. Punjabi, *J. Macromol. Sci., Part A: Pure Appl. Chem.*, 2015, **52**(2), 95–104.
- 60 A. G. Mustafin, L. R. Latypova, A. N. Andriianova, I. N. Mullagaliev, S. M. Salikhov, R. B. Salikhov and G. S. Usmanova, *RSC Adv.*, 2021, **11**(34), 21006–21016.
- 61 Y. Wang, G. H. Mazurek and E. C. Alocilja, *J. Electrochem. Soc.*, 2016, **163**(5), 140–145.
- 62 J. S. Yuka, J.-H. Jina, E. C. Alociljaa and J. B. Roseb, *J. Biosens. Bioelectron.*, 2009, **24**(5), 1348–1352.

